

# Posterior sampling for inverse imaging problems on the sphere

Augustin Marignier\*, Jason D. McEwen, Ana M.G. Ferreira, Thomas Kitching

**Abstract**—Inverse problems defined on the sphere arise in many fields, and are generally high-dimensional and computationally very complex. As a result, sampling the posterior of spherical inverse problems is a challenging task. In this work, we describe a framework that leverages a proximal Markov chain Monte Carlo algorithm to efficiently sample the high-dimensional space of spherical inverse problems with a sparsity-promoting wavelet prior. We detail the modifications needed for the algorithm to be applied to spherical problems, and give special consideration to the crucial forward modelling step which contains spherical harmonic transforms that are computationally expensive. By sampling the posterior, our framework allows for full and flexible uncertainty quantification, something which is not possible with other methods based on, for example, convex optimisation. We demonstrate our framework in practice on a common problem in global seismic tomography. We find that our approach is potentially useful for a wide range of applications at moderate resolutions.

**Index Terms**—Bayes methods, Monte Carlo methods, parameter estimation, uncertainty

## I. INTRODUCTION

INVERSE problems on the sphere are common in many fields, from astrophysics (e.g. [1,2]), to geophysics (e.g. [3,4]) and more. These tend to be high-dimensional and computationally challenging imaging problems, increasingly so at high resolutions. Spherical inverse problems are difficult to solve using posterior sampling methods such as Markov chain Monte Carlo (MCMC), largely due to the generally large number of parameters to sample and the high computational cost of repeated evaluations of the forward problem on the sphere. MCMC methods are widely used [5]–[10], benefitting from their ability to sample the full posterior probability density function (pdf) of the inverse problem, which allows for flexible calculation of any measure of uncertainty. Furthermore, they can be used to solve non-linear inverse problems, which are commonplace in, for example, geophysics [6,7,11]. This comes at significant computational cost, both in the posterior sampling (parameter inference) and calculation of the Bayesian evidence (marginal likelihood) for model comparison (the latter is often computationally infeasible). The simpler

MCMC methods, such as the Metropolis-Hastings (MH) algorithm, are known to struggle in high-dimensional parameter spaces (e.g. [12,13]), such as those for spherical inverse problems. The exponential increase in volume of the parameter space makes MH unable to converge to a solution. Alternative gradient-based methods such as the Hamiltonian Monte Carlo (HMC) [13] and the unadjusted Langevin algorithm (ULA) [14] scale favourably compared to the MH algorithm as the number of dimensions increases [12,13]. The caveat here is that these methods can only be applied to smooth distributions, limiting the form of prior information that can be used as regularisation.

Compressed sensing [15,16] has demonstrated that sparse signals can be accurately recovered from incomplete data, recovering both sharp and smooth image features simultaneously from underdetermined systems [17,18]. As a result, sparse priors have been widely adopted for solving inverse imaging problems, e.g. for radio interferometry applications [10,19]–[22], cosmological mass-mapping [23], and have received some attention in seismic tomography [17,24]. The prior pdf often used to promote sparsity is the Laplace distribution, which is non-differentiable and so cannot be used with gradient-based sampling algorithms.

Current approaches to uncertainty quantification for high-dimensional inverse problems with sparse regularisation exploit results from information theory to derive approximate credible regions from a single point estimate solution of the inverse problem [22,23,25]. The point estimate solution can be obtained using convex optimisation [22,23], and thus this approach is much faster than posterior sampling, particularly for high-resolution spherical problems. However, this information theory based approach can only approximate credible regions. While these can be used to quantify uncertainties in a variety of ways, the uncertainty quantification approaches that can be considered are highly restricted. Furthermore, the approximate nature of the approach means that pixel-level uncertainties can be overestimated, and hence local uncertainties are usually quantified in terms of superpixels i.e. sets of neighbouring pixels (e.g. [26]). A sampling method on the other hand will have the flexibility to calculate any measure of uncertainty, and will also give uncertainties at the pixel level.

In this work we provide a framework for solving inverse problems on the sphere using posterior sampling with sparsity-promoting priors. For this, we leverage a proximal MCMC algorithm [27], which is a sampling scheme that uses proximal mappings to efficiently sample high-dimensional parameter

\* Corresponding author. Email [augustin.marignier.14@ucl.ac.uk](mailto:augustin.marignier.14@ucl.ac.uk)

A. Marignier is supported by the STFC UCL Centre for Doctoral Training in Data Intensive Science (Grant Number ST/P006736/1).

A. Marignier, J. McEwen and T. Kitching are with the Mullard Space Science Laboratory, University College London, Surrey, RH5 6NT, UK.

A. Marignier and A.M.G. Ferreira are with the Department of Earth Sciences, University College London, London, WC1E 6BT, UK.

A.M.G. Ferreira is also with CERIS, Instituto Superior Técnico, Universidade de Lisboa, Lisboa, Portugal.

spaces. Proximal mappings can be viewed as more general gradient operators that can be used even on non-differentiable functions, allowing us to use a Laplace prior to promote sparsity. In our framework we outline the modifications needed to the proximal MCMC algorithm for spherical problems, with particular consideration given to the parameterisation and forward operator. We then demonstrate our framework in practice on a common problem from the field of global seismic tomography.

This paper is structured as follows. Section II gives the necessary mathematical background for Bayesian inference and representations of spherical images. Section III outlines our framework for posterior sampling of inverse problems on the sphere, with details of the proximal MCMC algorithm that we use. Section IV contains our illustrative example from global seismic tomography, and we conclude in Section V.

## II. MATHEMATICAL BACKGROUND

In this section we provide the necessary mathematical background for this work, including Bayesian inference for imaging, and harmonic and wavelet representations of spherical images.

### A. Bayesian inference for imaging

Consider some observed data  $\mathbf{d}$  and model parameters  $\mathbf{m}$  that are related by some general, possibly non-linear, forward operator  $\mathbf{G}$ , as

$$\mathbf{d} = \mathbf{G}(\mathbf{m}) + \mathbf{n}, \quad (1)$$

where  $\mathbf{n}$  represents observational noise. The aim of the inverse problem is to infer  $\mathbf{m}$  from  $\mathbf{d}$ . This can be formulated in a Bayesian statistical framework by Bayes Theorem as

$$p(\mathbf{m}|\mathbf{d}) \propto p(\mathbf{d}|\mathbf{m})p(\mathbf{m}). \quad (2)$$

Here  $p(\mathbf{m}|\mathbf{d})$  is known as the posterior pdf that encapsulates knowledge of the model parameters  $\mathbf{m}$  given data  $\mathbf{d}$  and represents the solution to the inverse problem [5,28]. The likelihood function  $p(\mathbf{d}|\mathbf{m})$ , assuming independent and identically distributed Gaussian noise with standard deviation  $\sigma$  in the data, is given by

$$p(\mathbf{d}|\mathbf{m}) \propto \exp\left(-\frac{\|\mathbf{d} - \mathbf{G}(\mathbf{m})\|_2^2}{2\sigma^2}\right). \quad (3)$$

Inverse problems are typically ill-posed and often require some form of regularisation in the form of prior knowledge about the model parameters. In the Bayesian framework, this is represented by the prior pdf  $p(\mathbf{m})$ , which can take many forms. Common examples include the Uniform prior [29],  $p(\mathbf{m}) \propto \text{constant}$ ; the Gaussian prior [28,30],  $p(\mathbf{m}) \propto \exp(-\mu\|\mathbf{m}\|_2^2)$ ; and the Laplace prior [15,16],  $p(\mathbf{m}) \propto \exp(-\mu\|\mathbf{m}\|_1)$ , to promote sparsity. In these priors,  $\|\cdot\|_p$  is the  $l_p$ -norm and  $\mu$  is a parameter that captures the width of the distribution. Henceforth we use the Laplace prior as we wish to promote sparsity. The constant of proportionality in (2) is known as the Bayesian evidence. This is useful for comparing the physical model ( $\mathbf{G}$ ) to alternative hypotheses, but may be ignored for inference about model parameters  $\mathbf{m}$ .

Solving the inverse problem by probabilistic sampling involves sampling the posterior pdf  $p(\mathbf{m}|\mathbf{d})$ , most commonly using MCMC algorithms. The simplest is the Metropolis-Hastings (MH) algorithm. MH proposes a new sample from a proposal distribution, which has a certain probability of being accepted. More sophisticated and better suited to high-dimensional problems than MH are gradient-based methods, such as the HMC and Langevin algorithms mentioned previously, which use the gradients of the target pdf to more efficiently guide the exploration of the parameter space. While the set of samples from the posterior pdf represents the full solution of the inverse problem, results are generally reported in terms of summary statistics, such as the mean of the samples, or the *maximum a posteriori* (MAP) solution,

$$\mathbf{m}^{(\text{MAP})} = \underset{\mathbf{m}}{\text{argmax}} p(\mathbf{m}|\mathbf{d}). \quad (4)$$

However, due to the randomness of MCMC there is no guarantee of the MAP being found, though the samples with the highest posterior probability should be quite close to it. Additionally, some measure of uncertainty on individual model parameters can be calculated from the posterior samples. We give further details of this in the next section.

The forward operator  $\mathbf{G}$  in (1) can be described as a (possibly non-linear) measurement operator  $\Phi$  acting on an image  $\mathbf{x}$ . In many physical situations, the image  $\mathbf{x}$  has a sparse representation in some basis, which can be exploited to regularise the inverse problem. For some sparsifying basis  $\Psi$ , we have  $\mathbf{x} = \Psi\alpha$ , where  $\alpha$  is the set of coefficients representing  $\mathbf{x}$  in the basis encoded in  $\Psi$ . The model parameters  $\mathbf{m}$  sampled by MCMC are the coefficients  $\alpha$ , and as such the forward operator is given by

$$\mathbf{G}(\alpha) = \Phi(\Psi\alpha). \quad (5)$$

For non-linear inverse problems, i.e. where  $\Phi$  is a non-linear measurement operator, a common choice is to linearise via a Taylor expansion around an initial guess model. While this usually leads to acceptable results in weakly non-linear problems, linearisation errors and the need for a good initial guess model can lead to artefacts in the recovered model. If the forward problem (5) is computationally fast, sampling methods are typically best for strongly non-linear problems.

### B. Harmonic representations of spherical images

We consider functions  $f(\theta, \phi)$  defined on the sphere  $\mathbb{S}^2$  with colatitude  $\theta \in [0, \pi]$  and longitude  $\phi \in [0, 2\pi)$ . The canonical orthogonal basis functions for  $\mathbb{S}^2$  are the spherical harmonics

$$Y_{lm}(\theta, \phi) = \sqrt{\frac{2\ell+1}{4\pi} \frac{(\ell-m)!}{(\ell+m)!}} P_\ell^m(\cos\theta) e^{im\phi} \quad (6)$$

for non-negative integers  $\ell$  and integers  $m \leq |\ell|$ , denoting angular degree and angular order, respectively. The spherical harmonics can be generalised for spin symmetries, but here we only consider spin-0 functions. As per the Condon-Shortley phase convention, the associated Legendre functions  $P_\ell^m(x)$  include a  $(-1)^m$  phase factor, ensuring the conjugate symme-

try relation

$$Y_{\ell,-m}(\theta, \phi) = (-1)^m Y_{\ell m}^*(\theta, \phi), \quad (7)$$

where  $*$  denotes complex conjugation. Any square integrable scalar function on  $\mathbb{S}^2$  can be represented in the frequency domain by its harmonic coefficients  $f_{\ell m} \in \mathbb{C}$ , obtained by projecting  $f$  onto the spherical harmonic basis functions using the inner product (forward spherical harmonic transform)

$$f_{\ell m} = \langle f, Y_{\ell m} \rangle = \int_{\mathbb{S}^2} f(\theta, \phi) Y_{\ell m}^*(\theta, \phi) \sin \theta d\theta d\phi. \quad (8)$$

The function  $f(\theta, \phi)$  can be recovered exactly from its spherical harmonic coefficients (inverse spherical harmonic transform) by

$$f(\theta, \phi) = \sum_{\ell=0}^{\infty} \sum_{m=-\ell}^{\ell} f_{\ell m} Y_{\ell m}(\theta, \phi). \quad (9)$$

In this work we consider bandlimited signals, that is signals such that  $f_{\ell m} = 0$ ,  $\forall \ell \geq L$  for some bandlimit  $L$ . We sample spherical signals according to the McEwen-Wiaux (MW) sampling theorem [31]. This equiangular sampling theorem has theoretically exact and efficient spherical harmonic transforms and requires fewer samples than other sampling theorems (e.g. [32,33]).

### C. Wavelet representations of spherical images

For our sparsifying basis, we consider scale-discretised axisymmetric wavelets [34]–[36], i.e., the wavelets are azimuthally symmetric when placed at the poles. There exist directional wavelets which vary azimuthally (e.g. [34,37]) and may be desirable in certain applications. However, such wavelets require transforms on the rotation group  $\text{SO}(3)$  which are typically than transforms on  $\mathbb{S}^2$ . The spherical wavelet transform is defined as the convolution of  $f$  and the wavelets  $\Psi^j(\theta, \phi)$ . Convolution on the sphere is defined as the inner product of  $f$  with wavelets that have been rotated over the surface of the sphere by some operator  $\mathcal{R}_{(\theta, \phi)}$ . As such, the wavelet coefficients  $W^{\Psi^j} \in \mathbb{S}^2$  are given by

$$W^{\Psi^j}(\theta, \phi) = \langle f, \mathcal{R}_{(\theta, \phi)} \Psi^j \rangle. \quad (10)$$

The wavelets  $\Psi^j$  cover a range of scales  $J_0 \leq j \leq J$ , which extract the highest frequency (high  $\ell$  information of  $f$ ). The lowest frequency information (low  $\ell$ ) is extracted by a scaling function  $\Phi(\theta, \phi)$  in a similar manner:

$$W^{\Phi}(\theta, \phi) = \langle f, \mathcal{R}_{(\theta, \phi)} \Phi \rangle. \quad (11)$$

The wavelets and scaling function are defined on the harmonic line such that they satisfy an admissibility condition which allows  $f$  to be decomposed and recovered exactly from its wavelet coefficients. The reconstruction is given by

$$f(\theta, \phi) = \sum_{\Gamma} \int_{\mathbb{S}^2} W^{\Gamma}(\theta', \phi') (\mathcal{R}_{(\theta', \phi')} \Gamma)(\theta, \phi) \sin \theta' d\theta' d\phi' \quad (12)$$

where  $\Gamma \in \{\Phi, \Psi^j\}$ . Note that in practice the spherical wavelet transform is computed in harmonic space [35], meaning the forward and inverse wavelet transforms (10-12) implicitly

involve both a forward and an inverse spherical harmonic transform [18]. The spherical harmonic and axisymmetric wavelet transforms used in this work are implemented in the packages `PYSSHT`<sup>1</sup> and `PYS2LET`<sup>2</sup>, respectively.

## III. FRAMEWORK FOR POSTERIOR SAMPLING ON THE SPHERE

In this section we outline our framework for sampling the posterior of spherical inverse problems. We give the details of the high-dimensional sampling algorithm we use and the modifications necessary for the sphere. Extra consideration is given to the forward operator, and finally we define a measure of uncertainty that can be calculated from the posterior samples.

### A. Proximal MCMC

1) *Moreau-Yosida envelope and proximal mapping*: The  $\lambda$ -Moreau-Yosida envelope of some concave function  $h(\mathbf{x})$  is given by [38,39]

$$h^{\lambda}(\mathbf{x}) = \min_{\mathbf{u}} \{h(\mathbf{u}) + \|\mathbf{u} - \mathbf{x}\|_2^2 / (2\lambda)\}, \quad (13)$$

where  $\lambda > 0$ . This is a smooth approximation of  $h$  with many desirable properties. Firstly,  $h^{\lambda}$  can be made arbitrarily close to  $h$  by making  $\lambda$  small. Secondly, the minimisers of  $h^{\lambda}$  are the same as the minimisers of  $h$ . Thirdly,  $h^{\lambda}$  is continuously differentiable even if  $h$  is not. The gradient of  $h^{\lambda}$  is given by

$$\nabla h^{\lambda}(\mathbf{x}) = [(\mathbf{x} - \text{prox}_h^{\lambda}(\mathbf{x}))]/\lambda, \quad (14)$$

where  $\text{prox}_h^{\lambda}(\mathbf{x})$  is the proximal mapping of  $h$  [38]

$$\text{prox}_h^{\lambda}(\mathbf{x}) = \underset{\mathbf{u}}{\text{argmin}} \{h(\mathbf{u}) + \|\mathbf{u} - \mathbf{x}\|_2^2 / (2\lambda)\}. \quad (15)$$

Rewriting (14) as

$$\text{prox}_h^{\lambda}(\mathbf{x}) = \mathbf{x} - \lambda \nabla h^{\lambda}(\mathbf{x}) \quad (16)$$

is reminiscent of the standard first-order finite differences approximation  $h(x_0 + a) \approx h(x_0) + ah'(x_0)$ , which shows that  $\text{prox}_h^{\lambda}$  may be interpreted as a gradient step in  $h^{\lambda}$  with step size  $\lambda$ , and can thus be used to minimise  $h^{\lambda}$  and, by extension,  $h$  [40]. For a concise review of proximal algorithms see [40], and [41] for a more detailed review.

2) *Proximal Langevin algorithm*: The proximal MCMC method developed by [27] is based on Langevin MCMC [14], a gradient-based sampling method, which we describe here. Consider a Langevin diffusion process  $Y(t)$  for  $0 \leq t \leq T$  associated with a stationary pdf  $\pi$ . This process is given by the stochastic differential equation

$$dY(t) = \frac{1}{2} \nabla \log \pi[Y(t)] dt + dW(t) \quad (17)$$

for some Brownian motion  $W$ . We use the forward Euler discrete time approximation with step size  $\delta$

$$\mathbf{m}^{(i+1)} = \mathbf{m}^{(i)} + \frac{\delta}{2} \nabla \log \pi[\mathbf{m}^{(i)}] + \sqrt{\delta} \mathbf{w}^{(i)}, \quad (18)$$

<sup>1</sup><https://github.com/astro-informatics/ssht>

<sup>2</sup><https://github.com/astro-informatics/s2let>

where  $\mathbf{m}$  is the discretised Langevin diffusion and  $\mathbf{w}^{(i)} \sim \mathcal{N}(0, \mathbb{I})$ . This is the Unadjusted Langevin Algorithm (ULA) [14]. Under certain regularity conditions, ULA produces samples that converge to an ergodic measure close to  $\pi$ . A MH acceptance step can be added to remove the approximation error, giving the Metropolis-Adjusted Langevin Algorithm (MALA) [14].

A well known limitation of the Langevin and other gradient-based sampling algorithms is that they require differentiable pdfs, which is not the case for some popular priors such as the Laplace prior. A proposed solution to this is to apply a Moreau-Yosida approximation to the non-differentiable terms in the posterior pdfs [10, 27, 42]. The posterior pdf for our inverse problem (2) is of the form  $\pi(\mathbf{m}) \propto \exp(-g(\mathbf{m}) - f(\mathbf{m}))$ , where  $g(\mathbf{m}) = \frac{1}{2\sigma^2} \|\mathbf{d} - \mathbf{G}(\mathbf{m})\|_2^2$  is our Gaussian data fidelity and  $f(\mathbf{m}) = \mu \|\mathbf{m}\|_1$  is our non-differentiable Laplacian prior. Applying a  $\lambda$ -Moreau-Yosida approximation to the prior, it then follows that the chain step for the Moreau-Yosida ULA (MYULA) is given by

$$\begin{aligned} \mathbf{m}^{(i+1)} &= \left(1 - \frac{\delta}{\lambda}\right) \mathbf{m}^{(i)} + \frac{\delta}{\lambda} \text{prox}_f^\lambda[\mathbf{m}^{(i)}] \\ &\quad - \delta \nabla g[\mathbf{m}^{(i)}] + \sqrt{\delta} \mathbf{w}^{(i)}. \end{aligned} \quad (19)$$

The tuning parameter  $\delta$  must be small for the forward Euler approximation (18) to converge, and [27] argued that the optimal value for  $\lambda$  is  $\lambda = \delta/2$ . We describe how to calculate the proximal mapping of our prior on the sphere (second term 19) in the following subsection. If  $\mathbf{G}$  is linear, the gradient of the data fidelity is straightforward to calculate using the adjoint

$$\nabla g = \mathbf{G}^\dagger (\mathbf{G}\mathbf{m} - \mathbf{d}) / \sigma^2. \quad (20)$$

It is straightforward to modify (20) if the data errors are characterised by a covariance matrix  $\mathbf{C}$  rather than a single standard deviation  $\sigma$ . It is important to note here that for spherical inverse problems, the forward operator  $\mathbf{G}$  may include spherical harmonic transforms, and thus the adjoint transforms are also needed for (20). Further discussion about  $\mathbf{G}$  in the spherical setting is given later in this section. Algorithm 1 outlines the use of the MYULA chain in practice, highlighting the key steps and equations. Again, a MH acceptance step can be added [10, 27], however in our experiments there was little improvement for the additional computational cost.

### B. Modification for the sphere

We sample a set of spherical wavelet coefficients that are defined at each point on the sphere (10). The MW sampling theorem is equiangular, and as such we need to account for an overdensity of sampling points near the poles when we calculate the proximal mapping of our sparsity-promoting prior. Proximal operators are generally calculated by a small convex optimisation problem [40]. Fortunately, there exist closed-form representations for the proximal mapping of many common functions [41], including the  $\ell_1$ -norm we use in our prior. This is crucial for MCMC methods where the proximal mapping needs to be repeatedly computed. It can be shown

---

### Algorithm 1 MYULA on the sphere

---

**INPUTS:** observed data  $\mathbf{d}$ , data errors  $\sigma$ , initial sample  $\mathbf{m}^{(0)}$ ,  $i = 0, N$ ,  $N_{\text{thin}}$ ,  $N_{\text{burn}}$ , quadrature weights  $\mathbf{q}$ ,  $\delta$ ,  $\lambda$ ,  $\mu$   
**OUTPUTS:** chain  $\{\mathbf{m}^{(i)} : i = 1, \dots, N\}$   
**while**  $i < N \times N_{\text{thin}} + N_{\text{burn}}$  **do**  
    Calculate gradient of data fidelity (eq 20)  
    Calculate proximity map of prior (eq 23)  
    Calculate  $\mathbf{m}^{(i+1)}$  (eq 19)  
    **if**  $i > N_{\text{burn}}$  **then**  
        **if**  $\text{mod}(i, N_{\text{thin}}) = 0$  **then**  
            Save  $\mathbf{m}^{(i+1)}$  to chain  
        **end if**  
    **end if**  
     $i += 1$   
**end while**

---

that for  $f(\mathbf{m}) = \mu \|\mathbf{m}\|_1$ ,

$$\text{prox}_f^\lambda(\mathbf{m}) = \text{soft}_{\lambda\mu}(\mathbf{m}) \quad (21)$$

where  $\text{soft}_T$  is the *soft thresholding* operator with threshold  $T$  defined as [41]

$$\text{soft}_T(m_i) = \begin{cases} 0 & \text{if } m_i \leq T, \\ m_i - T \text{sgn}(m_i) & \text{if } m_i > T \end{cases} \quad (22)$$

and can be applied component-wise to the components  $m_i$  of  $\mathbf{m}$ . Further, it can also be shown that for some linear transform operator  $\mathbf{A}$  that satisfies  $\mathbf{A}^\dagger \mathbf{A} = \nu \mathbf{I}$ , the proximal map of a function  $f(\mathbf{A}\mathbf{m})$  of the transformation is given by [41]

$$\text{prox}_f(\mathbf{A}\mathbf{m}) = \mathbf{m} + \nu^{-1} \mathbf{A}^\dagger (\text{prox}_{\nu f}[\mathbf{A}\mathbf{m}] - \mathbf{A}\mathbf{m}). \quad (23)$$

We can use (21) and (23) in combination to properly calculate the proximal mapping of the  $\ell_1$ -norm of a spherical signal. In this case, the linear transform in (23) is a diagonal matrix with quadrature weights [31] that vary with colatitude on the sphere along the main diagonal. As a result the threshold in (22) is larger at the equator than at the poles.

### C. The forward operator

A key consideration for any MCMC sampling algorithm is the speed of the forward modelling step, i.e. making predictions of the data  $\mathbf{d}$  given a MCMC sample  $\mathbf{m}$ . This is particularly important for spherical problems where the forward operator  $\mathbf{G}$  may contain spherical harmonic transforms, which are, unfortunately, slow and typically scale in complexity as  $\mathcal{O}(L^3)$  [31]. As discussed in Section II, the spherical harmonic transforms are implicit in the spherical wavelet transforms which form our sparsifying basis. Expanding (5) to see this, to sample the spherical wavelet coefficients in pixel space  $\alpha$  we have in practice

$$\mathbf{G}(\alpha) = \Phi \mathbf{S}^{-1} \mathbf{W} \mathbf{S} \alpha, \quad (24)$$

where  $\mathbf{S}$  and  $\mathbf{S}^{-1}$  are the forward and inverse spherical harmonic transforms (8 and 9), respectively, and  $\mathbf{W}$  is the spherical wavelet transform in harmonic space [18, 35]. This is further complicated by the need for the adjoints of these



transforms (20). These four spherical harmonic transforms at each MCMC step immediately limits the bandlimits  $L$  for which sampling the posterior may be feasible. For reference, in our experiments we performed dummy inversions at  $L = 64$  and  $L = 128$  with an identity measurement operator ( $\Phi = I$ ) which took around 3 and 17 days, respectively, for  $10^6$  samples on a 2.5 GHz Intel Xeon Platinum 8180M processor. While this may not be an issue for applications where information exists at relatively low degrees, for example in seismic tomography where maximum bandlimits are typically around  $L = 40$  (e.g. [3,4]), it will be impractical for applications where the bandlimits of interest are higher (e.g. [23]). To avoid spherical harmonic transforms in (24), one could instead sample the spherical harmonic coefficients of  $\alpha$ , provided one can reformulate the measurement operator  $\Phi$  appropriately. We note however that it is possible that, as shown in the following section, that the harmonic measurement operator may be slower than the pixel space operator even with spherical wavelet transforms. Further, it is conceivable that, depending on how the measurement operator scales, the choice of harmonic or pixel space will depend on the bandlimit  $L$ . If spherical harmonic transforms are unavoidable, it is crucial that these are computed as efficiently as possible, for example via repeated exploitation of fast Fourier transforms as in [31]. This all highlights the special consideration that must be given to the forward operator for spherical inverse problems.

#### D. Spherical wavelet parameterisation

As discussed in Section II, our inverse problem is parameterised using axisymmetric spherical wavelets [34,35,37] to promote sparsity. We can exploit the multiresolution character of these wavelets for further computational savings. By construction, the wavelets at each scale  $j$  each have different bandlimits  $k_j = B^{j+1} \leq L$ , where  $B$  is a wavelet scale parameter [35]. By using a sampling theorem, the transforms at each spherical wavelet scale can be performed up to their own bandlimit  $k_j$ , and only the minimum number of samples on the sphere at that bandlimit are needed. This multiresolution transform gives a four to five times speed up of the spherical wavelet transforms [35], and also dramatically reduces the dimensionality of our parameter space, compared to a full resolution transform where each wavelet scale is sampled at the overall bandlimit  $L$ . As an example, for parameters  $L = 32$ ,  $B = 2$ ,  $J_0 = 2$ , the full resolution algorithm has 10080 wavelet coefficients, compared to only 4676 for the multiresolution algorithm. While a full assessment of how this affects the convergence speed of the MCMC chain in terms of number of required steps is beyond the scope of this paper, we found real-time speed-ups and significant memory savings in our experiments.

#### E. Uncertainty quantification

By collecting samples from the posterior we can calculate any measure of uncertainty. For example, a common choice in Bayesian statistics is the credible intervals  $[\xi_i^-, \xi_i^+]$  of the model parameters. These intervals contain the values that can

be taken by parameter  $m_i$  with probability  $(1 - \alpha)$ , for some chosen small  $\alpha$

$$p(m_i \in [\xi_i^-, \xi_i^+] | \mathbf{d}) = 1 - \alpha \quad (25)$$

The lower and upper interval limits are calculated as the  $\frac{\alpha}{2}$  and  $1 - \frac{\alpha}{2}$  quantiles, respectively, of the posterior. We note that having sampled the spherical wavelet coefficients, inverse spherical wavelet transforms will be necessary to obtain an uncertainty map in real space as opposed to wavelet space. This can be expensive for the same reasons as previously discussed with respect to the forward operator, although to a much lesser extent after burn-in and thinned samples have been discarded. Of course if the desired summary statistic is linear in the model parameters (e.g. mean) then this can be calculated in wavelet space and only requires a single spherical wavelet transform. Importantly, in this way we get uncertainties at the pixel level when viewed in real space. As previously discussed, current uncertainty quantification methods in similar contexts only work on superpixels [26].

### IV. RECOVERING SURFACE WAVE PHASE VELOCITY MAPS

In this section we introduce the common problem in global seismic tomography of building surface wave phase velocity maps, which we use as an illustrative example. Being a 2-D problem that can be described by relatively simple theory, this is a natural example of application that is well suited to illustrate our framework for sampling the posterior for spherical inverse problems.

#### A. Surface wave phase velocity maps

Mapping the phase velocity of surface waves is a common problem in seismic tomography [43]–[45]. Seismic surface waves are dispersive, with different wave periods sampling different depths in the Earth's interior ([46]). Hence, creating these maps for waves of different periods is often a first step towards building 3D models of the Earth's mantle (e.g. [47]). Phase velocity is measured at a particular wave frequency for a particular source-receiver (i.e., earthquake to seismic station) pair. On global scales, long-period ( $T > 25$  s) phase velocity measurements are typically modelled using linearised ray theory, also known as the great-circle approximation (e.g. [48,49]) and inverted using least-squares algorithms (e.g. [28,43,45,47]). In this framework, the path travelled by the seismic wave is assumed to correspond to the great circle between the source and the receiver. The observed mean phase velocity anomaly  $\overline{\delta c/c_0}$  for a given source-receiver pair is given by the average of the phase velocity field along the minor arc great circle  $S$ ,

$$\overline{\delta c/c_0} = \frac{1}{\Delta} \int_S \frac{\delta c}{c_0}(\theta, \phi) dS, \quad (26)$$

where  $c_0$  is the phase velocity value computed for a reference Earth model, and  $\Delta$  is the length of path  $S$ .

Although there exist more complete theories describing phase velocity anomalies, notably including non-linear and finite frequency effects, recent studies have shown that the great-circle approximation accurately predicts the phase of long-period fundamental mode surface waves for current global

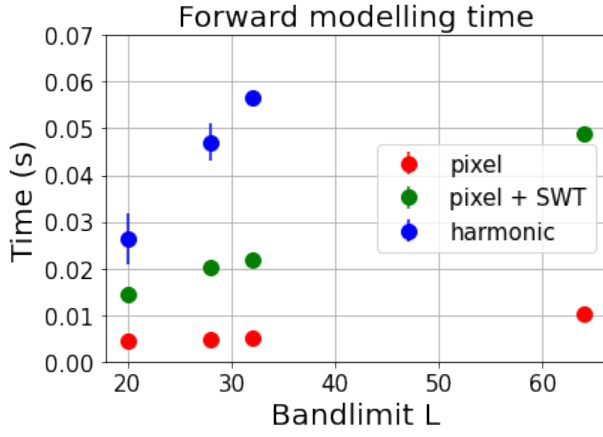


Fig. 1. Time taken to perform the forward modelling in pixel space (red), in pixel space with a spherical wavelet transform (green), and in harmonic space (blue). The point for the harmonic approach at bandlimit  $L = 64$  is well beyond the vertical scale at around 30 s. Timings performed on a 2017 MacBook Pro with 2.3 GHz Dual-Core Intel Core i5 processor.

tomography models (e.g. [49,50]). Hence, in this study we focus on the great-circle approximation. For simplicity we also only invert for isotropic lateral variations in phase velocity. We note, however, that our proximal MCMC approach can in principle handle these additional physical parameters (e.g. anisotropy) with some slight modification.

### B. Pixel space path integration

The common way to compute path integrals on the sphere (26) is to rotate the coordinate system such that the path lies along the equator, which is easily expressed in terms of Wigner-D matrices and the spherical harmonic coefficients of the spherical signal [46]. For a dataset with  $N_{\text{paths}}$  paths, the measurement operator can be represented by a dense matrix  $\Phi_h \in \mathbb{C}^{N_{\text{paths}} \times L^2}$  acting on the spherical harmonic coefficients  $\hat{x} \in \mathbb{C}^{L^2}$ . For seismic datasets typically consisting of  $\mathcal{O}(10^5)$  paths, this dense matrix multiplication can be quite slow. Our approach is to instead measure the path integral directly on the pixelised sphere using a sparse matrix  $\Phi_p \in \mathbb{R}^{N_{\text{paths}} \times N_{\text{pixels}}}$ , where each element of  $\Phi_p$  is a weight representing the normalised distance each path travels in a pixel. This effectively approximates the integral as a weighted Riemann sum over the pixelised function  $x \in \mathbb{R}^{N_{\text{pixels}}}$ . The adjoint operator is trivially the transpose of  $\Phi_p$ . The first step for our numerical path integration is to find discrete geographical points along the great circle minor arc between a source and a receiver using spherical trigonometry. For the discretisation, a sampling rate of about 200 points per radian (3.5 points per degree) was generally sufficient for this work. Each of the geographical points along the path is then mapped to its nearest MW sampling point. This mapping assigns a weight to each MW sampling point, which is given by

$$w_{tp} = \frac{n_{tp}}{s\Delta},$$

where  $n_{tp}$  is the number of geographical points on the path that are closest to MW sampling point indexed in the  $\theta$  and  $\phi$  directions by  $t$  and  $p$ , respectively,  $s$  is the path sampling rate

TABLE I  
ACCURACY OF PIXEL SPACE PATH INTEGRATION

| Bandlimit $L$ | Mean Diff. (%) | R2E                   |
|---------------|----------------|-----------------------|
| 20            | -0.01          | $2.14 \times 10^{-4}$ |
| 28            | -0.02          | $1.52 \times 10^{-4}$ |
| 32            | -0.02          | $1.34 \times 10^{-4}$ |
| 64            | -0.01          | $5.64 \times 10^{-5}$ |

and  $\Delta$  is the full path length. This can easily be done for each path of the dataset in parallel to build the full measurement operator.

Fig. 1 compares the forward modelling time for both the harmonic and pixel space path integrations,  $\Phi_h$  and  $\Phi_p$ , respectively, for bandlimits  $L \in \{20, 28, 32, 64\}$  and a realistic set of ray paths (see Fig. 3 bottom). Also shown are the times for the pixel space integration with an additional spherical wavelet transform  $\Phi_p\Psi$ , as required when sampling wavelet coefficients (5) instead of sampling the image directly. Clearly integration in pixel space is much faster than in harmonic space, even with the computational overhead of the spherical wavelet transforms. Pixel space integration also scales better to higher bandlimits. This is due to the extreme sparsity (less than 2% nonzero elements) of  $\Phi_p$ , whereas  $\Phi_h$  is generally dense. Table I shows the mean percentage difference and the relative squared error  $\text{R2E} = \|\mathbf{d}_{\text{harm}} - \mathbf{d}_{\text{pix}}\|_2^2 / \|\mathbf{d}_{\text{harm}}\|_2^2$  between predictions made in harmonic space,  $\mathbf{d}_{\text{harm}}$ , and in pixel space,  $\mathbf{d}_{\text{pix}}$ , when performed on the ground truth map we use in our synthetic experiment (see Fig. 2 top). As can be expected, as the bandlimit increases the error in the pixel space integration decreases. Crucially, even at relatively low bandlimits the pixel space integration is sufficiently accurate.

### C. Results

In this section we present the results of a synthetic test and real data inversions. We use MYULA to sample the axisymmetric wavelet coefficients  $\alpha$  of the spherical image  $\mathbf{x}$ , using the sparse measurement operator described in the previous section.

1) *Synthetic experiment:* As a synthetic example, we use the global phase velocity model GDM52 [45] at a wave period of  $T = 40$  s as a ground truth  $\mathbf{x}$ . Surface waves of this period are mainly sensitive to Earth structure at depths of around 100 km [46,47], so the image (Fig. 2) shows well-known tectonic features such as slow anomalies along spreading ridges (e.g. [45]). The model is bandlimited to  $L = 28$ . We create a synthetic dataset  $\mathbf{d}$  using our pixel-space forward operator  $\Phi$  and adding Gaussian random noise  $\mathbf{n} \sim \mathcal{N}(0, \sigma)$ , where  $\sigma$  is the standard deviation of the predictions  $\Phi\mathbf{x}$ .  $\Phi$  is constructed using the same paths as those used to originally build GDM52 [44,45], thereby ensuring a realistic and non-uniform spatial distribution of the data. In this case we have 179 657 paths. We use the signal-to-noise ratio

$$\text{SNR}(\mathbf{x}_0) = 20 \log_{10} \left( \frac{\|\mathbf{x}\|_2}{\|\mathbf{x} - \mathbf{x}_0\|_2} \right) \quad (27)$$

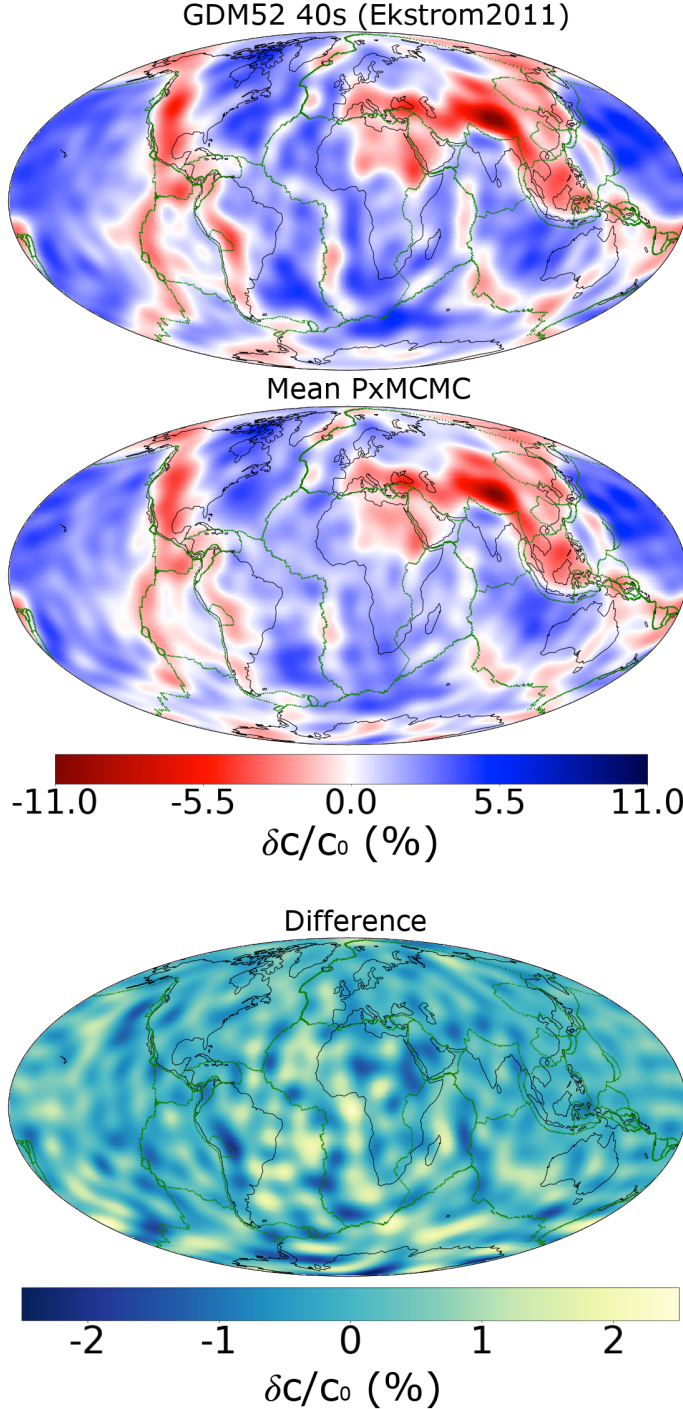


Fig. 2. Synthetic GDM52 recovery experiment. (top) Ground truth from [45]. (Middle) Mean solution from proximal MCMC. (Bottom) difference between the truth and our solution. All the maps show perturbations in phase velocity ( $\delta c/c_0$ ) with respect to the reference model PREM [51]. Green lines show the tectonic plate boundaries [52].

and relative squared error

$$\text{R2E}(\mathbf{x}_0) = \frac{\|\mathbf{d} - \Phi \mathbf{x}_0\|_2^2}{\|\mathbf{d}\|_2^2} \quad (28)$$

to assess the reconstruction accuracy and predictive accuracy, respectively, of our chosen point solution  $\mathbf{x}_0$ . We perform  $10^6$  MCMC steps, saving every 500<sup>th</sup> sample. The first half of the saved samples are discarded as a burn-in when calculating our mean solution and uncertainty. This takes the sampling well beyond the point of convergence, and takes about 20 hours on a 2.5 GHz Intel Xeon Platinum 8180M processor. The tuning parameters are set to  $\mu = 500$  and  $\delta = 10^{-6}$ . Fig. 2 shows the ground truth, the post-burn mean of our proximal MCMC samples and the difference between the two. Our solution has an excellent data fit ( $\text{R2E} = 9.96 \times 10^{-3}$ ) and model recovery ( $\text{SNR} = 8.81$  dB). Differences between the ground truth and our mean solution are small on average (0.5%) with some small-scale blobs of larger differences. The majority of these blobs occur in the southern hemisphere where data coverage is poorer (see Fig. 3).

We show the map of 95% credible interval ranges as well as a map showing the density of ray paths of our data set in Fig. 3. Here the uncertainty is calculated on the image space representation of our solution (i.e.  $\mathbf{x}$ ). As can be expected, on the whole we find lower uncertainties where we have a higher density of data in areas such as eastern Asia and western US. We also see much smaller scale regions of higher uncertainty. Looking at the uncertainties in wavelet space (i.e.  $\alpha$ , which is sampled by the proximal MCMC) in Fig. 4 it is clear that the smaller scale wavelet coefficients have higher uncertainty. Thus the patterns of differences between our chosen point solution and the truth (Fig. 2) are captured by the uncertainty of our sampled parameters.

2) *Real Data Inversions*: To demonstrate our method on real data, we invert the same data that was used to build GDM52 [44,45] at wave periods  $T = 25, 40, 75$  s, which have strong sensitivity to about 100 km, 160 km and 300 km depths, respectively [46,47]. The results of these inversions are shown in Fig. 5. The datasets at these wave periods consist of about 103 633, 179 657 and 286 302 paths, respectively. Again we use a bandlimit of  $L = 28$ . For these inversions, we perform 750 000 chain steps, saving every 500<sup>th</sup> sample and discarding the first 500 saved samples as burn-in. This takes between 8 and 33 hours, depending on the number of ray paths, on a 2.5 GHz Intel Xeon Platinum 8180M processor. The tuning parameter  $\delta$  is chosen on a case-by-case basis. Our mean solutions show all the expected velocity anomalies, being very similar to the GDM52 phase velocity maps (Fig. 5, left). For example, the  $T = 25$  s map (Fig. 5, top) shows a clear distinction between the slow continents and the fast oceans. On the other hand, the  $T = 40$  s map (Fig. 5, middle) depicts a good correlation between slow anomalies and plate boundaries, while the  $T = 75$  s map (Fig. 5, bottom) shows deeper mantle signals, such as high velocities associated with cratons. A notable difference with GDM52 (Fig. 5, left) is a north-south streak of fast velocities off the coast of the western US seen at all wave periods. This is a well-known artefact resulting from not modelling azimuthal anisotropy [45,53].



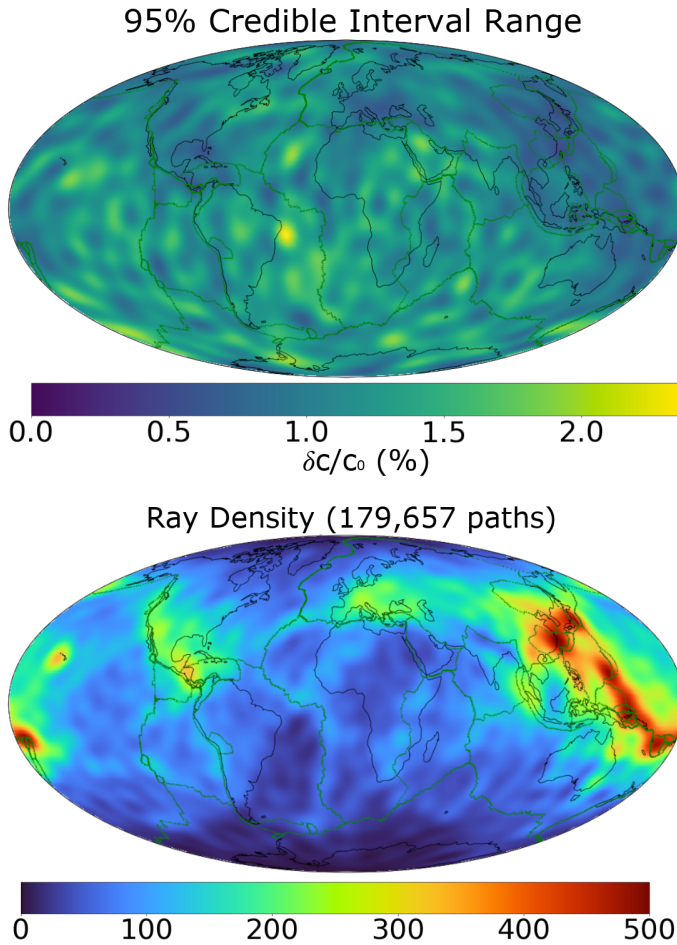


Fig. 3. Synthetic GDM52 recovery experiment. (top) 95% credible interval range (25) calculated on our MCMC samples in image space ( $\mathbf{x}$ ) in units of percentage deviation from the reference value, as in Fig. 2. (bottom) Row sum of path matrix  $\Phi$  (unitless) representing the density of rays in the dataset.

This streak corresponds to a region of high uncertainty in our solutions (Fig. 5, right). Again, the uncertainty maps correlate with ray density as expected.

We emphasise that the main purpose of this study is not to build improved phase velocity maps, which can be constructed quickly using, e.g. least squares approaches [28,43], but rather to illustrate and validate our framework for sampling the posterior of spherical inverse problems with a useful, well-known first application. Hence, we do not consider more sophisticated theoretical formulations, such as, e.g. full ray theory [54], finite frequency theory [55], including anisotropic effects [45], etc. Future work will focus on the application of the method to more sophisticated problems, such as e.g. depth inversions using non-linear theory.

## V. CONCLUSIONS

In this paper we have outlined a general framework for posterior sampling of inverse problems on the sphere with sparsity promoting priors that allows for flexible uncertainty quantification and extends naturally to non-linear problems. As with all MCMC methods, the suitability of this method

depends on the time taken to take the next chain sample, particularly in relation to the forward modelling step. The computational complexity of transforms on the sphere mean that this framework is generally feasible for problems of low to moderate resolution. At higher resolutions, posterior sampling quickly becomes intractable largely due to the poor scaling of spherical harmonic transforms present in the forward operator. In either case, special consideration must be given to the forward operator and whether it should be formulated in harmonic or pixel space, and also if its adjoint is known. A harmonic formulation would avoid repeated spherical harmonic transforms, but these savings could be lost on the measurement operator. Making use of a more efficient proximal algorithm based on a stochastic Runge-Kutta approximation of the Langevin equation [42] could be a promising way forward for higher resolution spherical inverse problems. This algorithm is more complex but converges to a solution much faster than the Euler approximation algorithm used in this work, thereby requiring fewer spherical harmonic transforms.

The surface wave phase velocity examples shown in this work are largely illustrative, as we have used the great circle approximation and not accounted for anisotropic effects, in which case a least-squares approach is fast and efficient. Nonetheless, our results demonstrate the feasibility of our framework methods on global scale tomographic inverse problems. In this case, the more commonly used harmonic formulation of the forward problem proved to be too slow, and we were able to reformulate it in pixel space such that it was much faster even with the computational overhead of spherical wavelet transforms. Further, the uncertainties calculated from our posterior samples make physical sense, being correlated with the distribution of data. Bayesian methods in seismic tomography on large-to-global scales have largely been used for independent 1D inversions (e.g. [56]–[58]), although new advances in gradient-based or variational methods (e.g. [59]–[62]) are promising for 2D and 3D probabilistic tomography. Our framework is a further contribution to this advance in methodology, with the novelty of being able to use a non-differentiable prior. Beyond seismology, our framework would be suitable for use in astrophysical applications at low- $\ell$  (e.g. [63]), climate modelling (e.g. [64]) and more.

## APPENDIX A CODE AND DATA AVAILABILITY

We provide a new Python package, `pypxmcmc`<sup>3</sup> that contains implementations of the proximal MCMC algorithms used in this work as well as the measurement operators, wavelet transforms and priors with their proximal mappings. The code is designed to be flexible, with base classes that will allow users to implement their own forward (measurement and transform) operators and priors. The proximal MCMC algorithms implemented are themselves not restricted to spherical problems, as the spherical aspects of the inversions appear in the likelihood and prior proximal calculations. We also provide scripts and data to reproduce the synthetic experiment described in this paper. MCMC chains for the real

<sup>3</sup><https://github.com/auggiemarignier/pxmcmc>



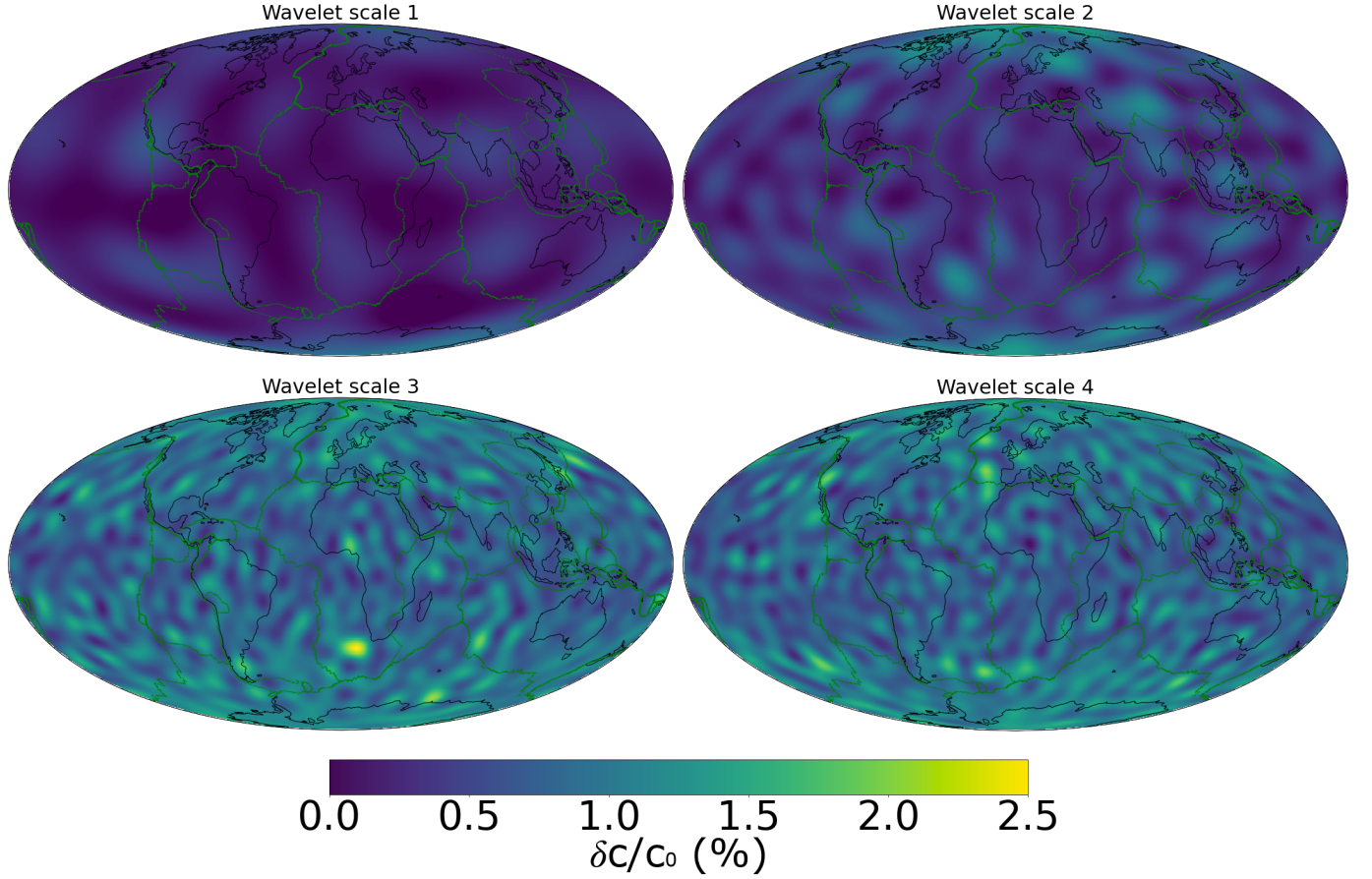


Fig. 4. Synthetic GDM52 recovery experiment. 95% credible interval ranges of spherical wavelet coefficients at different scales. The range of the colourbar is the same for all maps in units of percentage deviation from the reference value, as in Fig. 2 and 3.

data inversions are available from the authors upon request. The discretisation of great circle paths is implemented in our Python code `greatcirclepaths`<sup>4</sup>, which is publicly available.

#### ACKNOWLEDGEMENT

The authors would like to thank...

#### REFERENCES

- [1] Planck Collaboration, “Planck 2015 results - I. Overview of products and scientific results,” *Astron. Astrophys.*, vol. 594, p. A1, 2016.
- [2] N. Jeffrey, M. Gatti, C. Chang, L. Whiteway, U. Demirbozan, A. Kovacs, G. Pollina, D. Bacon, N. Hamaus, T. Kacprzak, O. Lahav, F. Lanusse *et al.*, “Dark energy survey year 3 results: Curved-sky weak lensing mass map reconstruction,” *Mon. Not. R. Astron. Soc.*, 2021.
- [3] J. Ritsema, A. Deuss, H. J. van Heijst, and J. H. Woodhouse, “S40RTS: a degree-40 shear-velocity model for the mantle from new Rayleigh wave dispersion, teleseismic traveltime and normal-mode splitting function measurements,” *Geophys. J. Int.*, vol. 184, no. 3, pp. 1223–1236, 2011.
- [4] S.-J. Chang, A. M. G. Ferreira, J. Ritsema, H. J. van Heijst, and J. H. Woodhouse, “Joint inversion for global isotropic and radially anisotropic mantle structure including crustal thickness perturbations,” *J. Geophys. Res.-Sol. Ea.*, vol. 120, no. 6, pp. 4278–4300, 2015.
- [5] K. Mosegaard and A. Tarantola, “Monte Carlo sampling of solutions to inverse problems,” *J. Geophys. Res.-Sol. Ea.*, vol. 100, no. B7, pp. 12 431–12 447, 1995.
- [6] A. Malinverno, “Parsimonious Bayesian Markov chain Monte Carlo inversion in a nonlinear geophysical problem,” *Geophys. J. Int.*, vol. 151, no. 3, pp. 675–688, 12 2002.
- [7] T. Bodin, M. Sambridge, K. Gallagher, and N. Rawlinson, “Transdimensional inversion of receiver functions and surface wave dispersion,” *J. Geophys. Res.-Sol. Ea.*, vol. 117, no. B2, 2012.
- [8] A. Lewis and S. Bridle, “Cosmological parameters from CMB and other data: A Monte Carlo approach,” *Phys. Rev. D*, vol. 66, p. 103511, Nov 2002.
- [9] V. L. Corless, L. J. King, and D. Clowe, “A new look at massive clusters: weak lensing constraints on the triaxial dark matter haloes of A1689, A1835 and A2204,” *Mon. Not. R. Astron. Soc.*, vol. 393, no. 4, pp. 1235–1254, 02 2009.
- [10] X. Cai, M. Pereyra, and J. D. McEwen, “Uncertainty quantification for radio interferometric imaging - I. Proximal MCMC methods,” *Mon. Not. R. Astron. Soc.*, vol. 480, no. 3, pp. 4154–4169, 2018.
- [11] A. M. G. Ferreira, A. Marignier, J. Attanayake, M. Frietsch, and A. Berbellini, “Crustal structure of the Azores Archipelago from Rayleigh wave ellipticity data,” *Geophys. J. Int.*, vol. 221, no. 2, pp. 1232–1247, 02 2020.
- [12] G. O. Roberts and J. S. Rosenthal, “Optimal scaling of discrete approximations to Langevin diffusions,” *J. Roy. Stat. Soc. B*, vol. 60, no. 1, pp. 255–268, 1998.
- [13] R. M. Neal, “MCMC using Hamiltonian dynamics,” in *Handbook of Markov Chain Monte Carlo*. CRC Press, 2012, pp. 113–162.
- [14] G. O. Roberts and R. L. Tweedie, “Exponential Convergence of Langevin Distributions and Their Discrete Approximations,” *Bernoulli*, vol. 2, no. 4, pp. 341–363, 1996.
- [15] D. L. Donoho, “Compressed sensing,” *IEEE Trans. Inf. Theory*, vol. 52, no. 4, pp. 1289–1306, 2006.
- [16] E. J. Candès, Y. C. Eldar, D. Needell, and P. Randall, “Compressed sens-

<sup>4</sup><https://github.com/auggiemarignier/GreatCirclePaths>

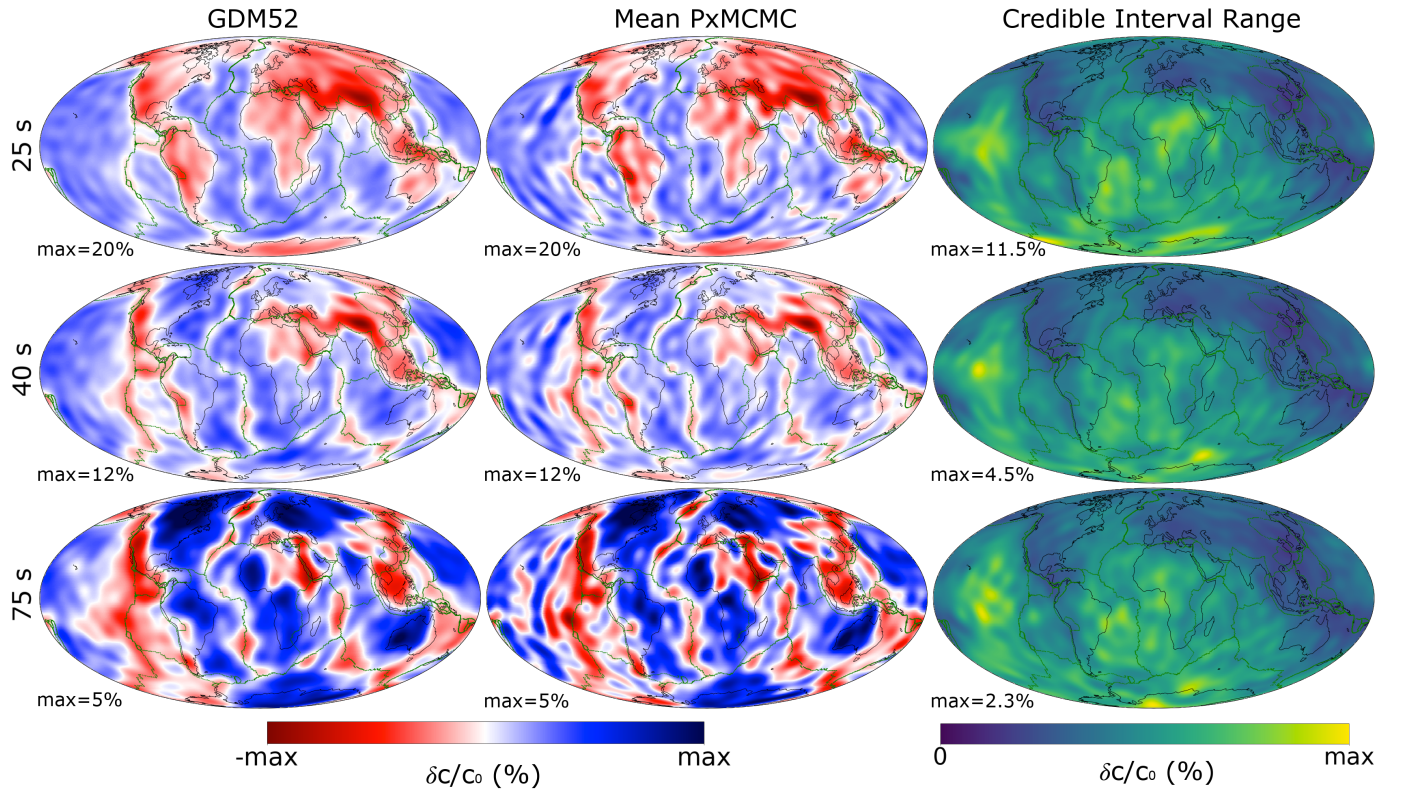


Fig. 5. Real data inversions. Phase velocity maps from GDM52 [45] (left), mean proximal MCMC solutions from this study (middle) and credible interval ranges (right) for wave periods 25, 40 and 75 s (top to bottom). All the maps show perturbations in phase velocity ( $\delta c/c_0$ ) with respect to the reference model PREM [51].

- ing with coherent and redundant dictionaries,” *Appl. Comput. Harmon.*, vol. 31, no. 1, p. 5973, 2011.
- [17] I. Loris, G. Nolet, I. Daubechies, and F. A. Dahlen, “Tomographic inversion using  $\ell_1$ -norm regularization of wavelet coefficients,” *Geophys. J. Int.*, vol. 170, no. 1, pp. 359–370, 2007.
- [18] C. G. Wallis, Y. Wiaux, and J. D. McEwen, “Sparse image reconstruction on the sphere: Analysis and synthesis,” *IEEE Trans. Image Process.*, vol. 26, no. 11, pp. 5176–5187, 2017.
- [19] Y. Wiaux, L. Jacques, G. Puy, A. M. M. Scaife, and P. Vanderghynst, “Compressed sensing imaging techniques for radio interferometry,” *Mon. Not. R. Astron. Soc.*, vol. 395, no. 3, pp. 1733–1742, 2009.
- [20] R. E. Carrillo, J. D. McEwen, and Y. Wiaux, “PURIFY: a new approach to radio-interferometric imaging,” *Mon. Not. R. Astron. Soc.*, vol. 439, no. 4, pp. 3591–3604, 2014.
- [21] L. Pratley, J. D. McEwen, M. d’Avezac, R. E. Carrillo, A. Onose, and Y. Wiaux, “Robust sparse image reconstruction of radio interferometric observations with purify,” *Mon. Not. R. Astron. Soc.*, vol. 473, no. 1, pp. 1038–1058, 09 2017.
- [22] X. Cai, M. Pereyra, and J. D. McEwen, “Uncertainty quantification for radio interferometric imaging: li. map estimation,” *Mon. Not. R. Astron. Soc.*, vol. 480, no. 3, pp. 4170–4182, 2018.
- [23] M. A. Price, J. D. McEwen, L. Pratley, and T. D. Kitching, “Sparse Bayesian mass-mapping with uncertainties: Full sky observations on the celestial sphere,” *Mon. Not. R. Astron. Soc.*, vol. 500, no. 4, pp. 5436–5452, 11 2020.
- [24] J. Charl  ty, S. Voronin, G. Nolet, I. Loris, F. J. Simons, K. Sigloch, and I. C. Daubechies, “Global seismic tomography with sparsity constraints: Comparison with smoothing and damping regularization,” *J. Geophys. Res.-Sol. Ea.*, vol. 118, no. 9, pp. 4887–4899, 2013.
- [25] M. Pereyra, “Maximum-a-posteriori estimation with bayesian confidence regions,” *SIAM J. Imaging. Sci.*, vol. 10, no. 1, pp. 285–302, 2017.
- [26] M. A. Price, X. Cai, J. D. McEwen, M. Pereyra, and T. D. Kitching, “Sparse bayesian mass mapping with uncertainties: local credible intervals,” *Mon. Not. R. Astron. Soc.*, vol. 492, no. 1, pp. 394–404, 2020.
- [27] M. Pereyra, “Proximal Markov chain Monte Carlo algorithms,” *Stat. Comput.*, vol. 26, no. 4, pp. 745–760, 2016.
- [28] A. Tarantola and B. Valette, “Generalized nonlinear inverse problems solved using the least squares criterion,” *Rev. Geophys. Space Ge.*, vol. 20, no. 1, pp. 219–232, 1982.
- [29] E. T. Jaynes, *Probability Theory: The Logic of Science*. Cambridge: Cambridge University Press, 2003.
- [30] G. H. Golub, P. C. Hansen, and D. P. O’Leary, “Tikhonov regularization and total least squares,” *SIAM J. Matrix Anal. A.*, vol. 21, no. 1, pp. 185–194, 1999.
- [31] J. D. McEwen and Y. Wiaux, “A novel sampling theorem on the sphere,” *IEEE Trans. Signal Process.*, vol. 59, no. 12, pp. 5876–5887, 2011.
- [32] J. R. Driscoll and D. M. Healy, “Computing Fourier Transforms and Convolutions on the 2-Sphere,” *Adv. Appl. Math.*, vol. 15, no. 2, p. 202250, Jun. 1994.
- [33] K. M. G  rski, E. Hivon, A. J. Banday, B. D. Wandelt, F. K. Hansen, M. Reinecke, and M. Bartelmann, “HEALPix: A Framework for High-Resolution Discretization and Fast Analysis of Data Distributed on the Sphere,” *Astrophys. J.*, vol. 622, no. 2, pp. 759–771, Apr. 2005.
- [34] Y. Wiaux, J. D. McEwen, P. Vanderghynst, and O. Blanc, “Exact reconstruction with directional wavelets on the sphere,” *Mon. Not. R. Astron. Soc.*, vol. 388, no. 2, pp. 770–788, 07 2008.
- [35] Leistedt, B., McEwen, J. D., Vanderghynst, P., and Wiaux, Y., “S2LET: A code to perform fast wavelet analysis on the sphere,” *Astron. Astrophys.*, vol. 558, p. A128, 2013.
- [36] J. D. McEwen, C. Durastanti, and Y. Wiaux, “Localisation of directional scale-discretised wavelets on the sphere,” *Applied and Computational Harmonic Analysis*, vol. 44, no. 1, pp. 59–88, 2018.
- [37] J. D. McEwen, B. Leistedt, M. Bttner, H. V. Peiris, and Y. Wiaux, “Directional spin wavelets on the sphere,” *IEEE Trans. Sig. Proc.*, submitted, 2015.
- [38] J. J. Moreau, “Fonctions convexes duales et points proximaux dans un espace hilbertien,” *CR Hebd. Acad. Sci.*, vol. 255, pp. 2897–2899, 1962.
- [39] H. H. Bauschke and P. L. Combettes, *Convex Analysis and Monotone*

- Operator Theory in Hilbert Spaces.* New York, NY: Springer New York, 2017.
- [40] N. Parikh and S. Boyd, “Proximal algorithms,” *Found. Trends Opt.*, vol. 1, no. 3, pp. 127–239, 2014.
  - [41] P. L. Combettes and J.-C. Pesquet, *Proximal Splitting Methods in Signal Processing.* New York, NY: Springer New York, 2011, pp. 185–212.
  - [42] M. Pereyra, L. V. Miele, and K. C. Zygalakis, “Accelerating Proximal Markov Chain Monte Carlo by Using an Explicit Stabilized Method,” *SIAM J. Imaging. Sci.*, vol. 13, no. 2, pp. 905–935, 2020.
  - [43] J. Trampert and J. H. Woodhouse, “Global phase velocity maps of Love and Rayleigh waves between 40 and 150 seconds,” *Geophys. J. Int.*, vol. 122, no. 2, pp. 675–690, 1995.
  - [44] G. Ekström, J. Tromp, and E. W. F. Larson, “Measurements and global models of surface wave propagation,” *J. Geophys. Res.-Sol. Ea.*, vol. 102, no. B4, pp. 8137–8157, 1997.
  - [45] G. Ekström, “A global model of Love and Rayleigh surface wave dispersion and anisotropy, 25–250 s,” *Geophys. J. Int.*, vol. 187, no. 3, pp. 1668–1686, 2011.
  - [46] F. A. Dahlen and J. Tromp, *Theoretical Global Seismology.* Princeton University Press, 1998.
  - [47] S. Durand, E. Debayle, and Y. Ricard, “Rayleigh wave phase velocity and error maps up to the fifth overtone,” *Geophys. Res. Lett.*, vol. 42, no. 9, pp. 3266–3272, 2015.
  - [48] J. H. Woodhouse and A. M. Dziewonski, “Mapping the upper mantle: Three-dimensional modeling of earth structure by inversion of seismic waveforms,” *J. Geophys. Res.-Sol. Ea.*, vol. 89, no. B7, pp. 5953–5986, 1984.
  - [49] L. Parisi and A. M. G. Ferreira, “Empirical assessment of the validity limits of the surface wave full ray theory using realistic 3-D Earth models,” *Geophys. J. Int.*, vol. 205, no. 1, pp. 146–159, 2016.
  - [50] K. E. Godfrey, C. A. Dalton, Z. Ma, V. Hjörleifsdóttir, and G. Ekström, “A comparison of approaches for the prediction and inversion of surface wave phase delays,” *Geophys. J. Int.*, vol. 217, no. 3, pp. 1496–1514, 2019.
  - [51] A. M. Dziewonski and D. L. Anderson, “Preliminary reference earth model,” *Phys. Earth Planet. In.*, vol. 25, no. 4, pp. 297–356, 1981.
  - [52] P. Bird, “An updated digital model of plate boundaries,” *Geochem. Geophys. Geosy.*, vol. 4, no. 3, 2003.
  - [53] D. W. Forsyth, “The early structural evolution and anisotropy of the oceanic upper mantle,” *Geophys. J. Int.*, vol. 43, no. 1, pp. 103–162, 1975.
  - [54] A. M. G. Ferreira and J. H. Woodhouse, “Source, path and receiver effects on seismic surface waves,” *Geophys. J. Int.*, vol. 168, no. 1, pp. 109–132, 2007.
  - [55] Y. Zhou, F. A. Dahlen, G. Nolet, and G. Laske, “Finite-frequency effects in global surface-wave tomography,” *Geophys. J. Int.*, vol. 163, no. 3, pp. 1087–1111, 2005.
  - [56] N. M. Shapiro and M. H. Ritzwoller, “Monte-Carlo inversion for a global shear-velocity model of the crust and upper mantle,” *Geophys. J. Int.*, vol. 151, no. 1, pp. 88–105, 2002.
  - [57] A. Khan, L. Boschi, and J. A. D. Connolly, “Mapping the Earth’s thermochemical and anisotropic structure using global surface wave data,” *J. Geophys. Res.-Sol. Ea.*, vol. 116, no. B1, 2011.
  - [58] M. Ravenna and S. Lebedev, “Bayesian inversion of surface-wave data for radial and azimuthal shear-wave anisotropy, with applications to central Mongolia and west-central Italy,” *Geophys. J. Int.*, vol. 213, no. 1, pp. 278–300, 11 2017.
  - [59] A. Fichtner, A. Zunino, and L. Gebraad, “Hamiltonian Monte Carlo solution of tomographic inverse problems,” *Geophys. J. Int.*, vol. 216, no. 2, pp. 1344–1363, 11 2018.
  - [60] L. Gebraad, C. Boehm, and A. Fichtner, “Bayesian Elastic FullWaveform Inversion Using Hamiltonian Monte Carlo,” *J. Geophys. Res.-Sol. Ea.*, vol. 125, no. 3, 2020.
  - [61] X. Zhang and A. Curtis, “Variational full-waveform inversion,” *Geophys. J. Int.*, vol. 222, no. 1, pp. 406–411, 2020.
  - [62] X. Zhao, A. Curtis, and X. Zhang, “Bayesian seismic tomography using normalizing flows,” *eartharxiv*, 2020.
  - [63] S. Plaszczyński, A. Lavabre, L. Perotto, and J. L. Starck, “A hybrid approach to cosmic microwave background lensing reconstruction from all-sky intensity maps,” *Astron. Astrophys.*, vol. 544, 2012.
  - [64] D. Foster, D. Comeau, and N. M. Urban, “A Bayesian Approach to Regional Decadal Predictability: Sparse Parameter Estimation in High-Dimensional Linear Inverse Models of High-Latitude Sea Surface Temperature Variability,” *J. Climate*, vol. 33, no. 14, 2020.